

Quantifying distortions of the Lagrangian dark-matter mesh in cosmology

Mark C. Neyrinck¹

¹*Department of Physics and Astronomy, The Johns Hopkins University, Baltimore, MD 21218, USA*

11 November 2018

ABSTRACT

We examine the Lagrangian divergence of the displacement field, arguably a more natural object than the density in a Lagrangian description of cosmological large-scale structure. This quantity, which we denote ψ , quantifies the stretching and distortion of the initially homogeneous lattice of dark-matter particles in the universe. ψ encodes similar information as the density, but the correspondence has subtleties. It corresponds better to the log-density A than the overdensity δ . A Gaussian distribution in ψ produces a distribution in A with slight skewness; in δ , we find that in many cases the skewness is further increased by 3.

A local spherical-collapse-based (SC) fit found by Bernardeau gives a formula for ψ 's particle-by-particle behavior that works quite well, better than applying Lagrangian perturbation theory (LPT) at first or second (2LPT) order. In 2LPT, there is a roughly parabolic relation between initial and final ψ that can give overdensities in deep voids, so low-redshift, high-resolution 2LPT realizations should be used with caution. The SC fit excels at predicting ψ until streams cross; then, for particles forming haloes, ψ plummets as in a waterfall to -3 . This gives a new method for producing N -particle realizations. Compared to LPT realizations, such SC realizations give reduced stream-crossing, and better visual and 1-point-PDF correspondence to the results of full gravity. LPT, on the other hand, predicts large-scale flows and the large-scale power-spectrum amplitude better, unless an empirical correction is added to the SC formula.

Key words: large-scale structure of Universe – cosmology: theory

1 INTRODUCTION

In the present, quite observationally successful theory of cosmology, the universe began with nearly uniform density everywhere. According to the theory of inflation, the small fluctuations in it began as tiny quantum fluctuations, that ‘inflated’ to macroscopic size as the universe ballooned in its first instants.

In an Eulerian description, the density and velocity fields at fixed comoving positions describe this process of structure formation. In a Lagrangian description, on the other hand, the fundamental object is the displacement field, a vector field measuring the comoving distance particles have traveled from their initial positions. Fluctuations are not fundamentally in the density, but in the separations between particles. If the particles are arranged on a cubic lattice, as they often are in N -body simulations, the density fluctuations are really deformations of this lattice. In underdense regions, the lattice stretches out; in overdense regions, it bunches together and forms structures.

While the density is still relevant in a Lagrangian framework (as it sources gravity), the simplest scalar to construct from the displacement field (besides its magnitude, which is irrelevant for local physics) is its Lagrangian divergence. We denote this divergence as ψ . It is the lowest-order invariant (with respect to rotations and translations) of the tidal tensor of the displacement field, and quan-

tifies the angle-averaged stretching of the Lagrangian sheet in comoving coordinates. Where a mass element becomes stretched out, ψ increases, and its density decreases. For a potential displacement field (i.e. with zero curl), ψ carries all of its information.

Lagrangian dynamics have long been applied to cosmology, going back at least to Zel’dovich (1970). It can be insightful to envision the process of structure formation in terms of the dynamics of a Lagrangian ‘sheet,’ a viewpoint that for instance has been applied to classify the types of caustics (folds of this sheet) that can form (e.g. Arnold et al. 1982; Arnold 2001). This viewpoint has gotten some attention recently (e.g. Shandarin et al. 2012; Abel et al. 2011; Falck et al. 2012b; Neyrinck 2012). The ‘sheet’ is initially flat in six-dimensional position-velocity phase space, with vanishing bulk velocity everywhere as the cosmic scale factor $a \rightarrow 0$. Seen in position space, gravity stretches out the sheet in underdense regions, and bunches it together in overdense regions. Assuming cold dark matter, the sheet never intersects itself in six-dimensional phase space, and instead folds up in rough analogy to origami.

Several modifications to the original Zel’dovich approximation (ZA) were proposed, including higher-order Lagrangian perturbation theory (LPT). In LPT, streams of matter typically overcross in high-density regions, failing to form the bound structures that they would in full gravity. Several modifications of LPT (e.g.

arXiv:1204.1326v2 [astro-ph.CO] 18 Sep 2012

Coles et al. 1993; Melott et al. 1994, and references therein) have been proposed to solve this problem, another attempted solution for which also occurs in the present paper. The adhesion model, for instance (Kofman & Shandarin 1988; Kofman et al. 1992; Shandarin 2009; Valageas & Bernardeau 2011; Hidding et al. 2012) prevents stream crossing by introducing an effective viscosity, allowing the structure to be predicted in an elegant geometrical fashion. There are other ways of producing approximate particle realizations in a Lagrangian perturbation-theory approach, e.g. the PINOCCHIO algorithm (Monaco et al. 2002).

One might argue that N -body simulations have become computationally cheap enough that such approximate realizations have little use. For example, though, such techniques have proven quite useful in Bayesian initial-conditions reconstruction (Kitaura & Angulo 2012; Jasche & Wandelt 2012), where full N -body simulations would be far too slow.

In this paper, we explore the behavior and properties of the Lagrangian spatial-stretching parameter ψ . In Section 2, we review several approximations for ψ in the literature and its relationship to the density field. In Section 3, we explore the relationship between ψ and density variables (the overdensity and the log-density) in a class of ‘local Lagrangian’ toy models, including a spherical collapse (SC) approximation that is most relevant to structure formation. In Section 4, we compare these approximations to results from an N -body simulation, demonstrating the success of the SC approximation. In Section 5, we test a simple new way of producing particle realizations using the SC approximation, and compare it to LPT approaches.

2 APPROXIMATIONS FOR THE DISPLACEMENT DIVERGENCE

There are several analytical approximations in the literature for the Lagrangian divergence of the displacement field. Where \mathbf{q} is a Lagrangian coordinate of a particle, we denote the displacement field as $\Psi(\mathbf{q}) = \mathbf{x}(\mathbf{q}) - \mathbf{q}$ (with \mathbf{x} the Eulerian position of a particle), and $\psi(\mathbf{q}) \equiv \nabla_{\mathbf{q}} \cdot \Psi(\mathbf{q})$. Here $(\nabla_{\mathbf{q}} \cdot)$ is the divergence operator in Lagrangian coordinates. Assuming that Ψ is a potential field, $\psi(\mathbf{q}) = \nabla_{\mathbf{q}}^2 \phi(\mathbf{q})$, where ϕ is the displacement potential. All of the approximations used in this paper assume that Ψ is a potential field, which implies that ψ contains all of the information in Ψ . In this section, we examine a few of these approximations. In full gravity, Ψ is not potential, i.e. it has a nonzero curl. However, as we show below, much of the large-scale clustering is captured with the potential-flow assumption.

2.1 Lagrangian Perturbation Theory

The Zel’dovich approximation (Zel’dovich 1970, ZA) is the first-order, linear approximation in Lagrangian perturbation theory (LPT). The ZA gives

$$\psi_{\text{lin}}(\mathbf{q}, \tau) = -\delta_{\text{lin}}(\mathbf{q}, \tau) = -\frac{D_1(\tau)}{D_1(\tau_0)} \delta_{\text{lin}}(\mathbf{q}, \tau_0), \quad (1)$$

where δ_{lin} is the overdensity linearly extrapolated with the linear growth factor D_1 , and τ_0 is some initial time.

The second-order (2LPT) expression is more complicated, but still straightforward to implement. This slight added complexity seems worth the trouble for initial-conditions generation (Scoccimarro 1998; Crocce et al. 2006; Tatekawa & Mizuno 2007; McCul-

lagh & Jeong in prep), giving much-reduced ‘transients’ compared to ZA-produced initial conditions.

At second order,

$$\psi_{2\text{LPT}}(\mathbf{q}) = \nabla_{\mathbf{q}}^2 \phi = -D_1 \nabla_{\mathbf{q}}^2 \phi^{(1)} + D_2 \nabla_{\mathbf{q}}^2 \phi^{(2)}, \quad (2)$$

where $\phi(\mathbf{q})$ is the total displacement potential, and D_2 is the second-order growth factor. $D_2(\tau) \approx -\frac{3}{7} D_1^2(\tau)$, the approximation holding to better than 2.6 percent for $0.1 < \Omega_m < 1$ (Bouchet et al. 1995). These first- and second-order potentials are

$$\nabla_{\mathbf{q}}^2 \phi^{(1)}(\mathbf{q}) = \delta_{\text{lin}}(\mathbf{q}), \quad (3)$$

$$\nabla_{\mathbf{q}}^2 \phi^{(2)}(\mathbf{q}) = \sum_{i>j} \left\{ \phi_{,ii}^{(1)}(\mathbf{q}) \phi_{,jj}^{(1)}(\mathbf{q}) - \left[\phi_{,ij}^{(1)}(\mathbf{q}) \right]^2 \right\}. \quad (4)$$

We introduce here an isotropic, parabolic approximation to 2LPT, $\psi_{2\text{LPT,parab}}$, for $\psi_{2\text{LPT}}$. Note that (suppressing the ⁽¹⁾ superscripts)

$$\sum_{i>j} (\phi_{,ii} \phi_{,jj}) = \frac{1}{2} \left[(\nabla_{\mathbf{q}}^2 \phi)^2 - \sum_i \phi_{,ii}^2 \right]. \quad (5)$$

Also note that in 3D, $\sum_i \phi_{,ii}^2$ is bounded by $\frac{1}{3} (\nabla_{\mathbf{q}}^2 \phi)^2$ (in the isotropic case that $\phi_{,ii}$ are equal for all i), and $(\nabla_{\mathbf{q}}^2 \phi)^2$ (in the case that $\phi_{,ii} = \nabla_{\mathbf{q}}^2 \phi$ for some i , with all other components zero). Putting this together, with $1/6$ (the isotropic case) $\geq c_2 \geq 1/2$, and recalling that $D_2 < 0$,

$$\psi_{2\text{LPT}}(\mathbf{q}) = -D_1 \delta + D_2 \left[c_2 \delta^2 - \sum_{i>j} (\phi_{,ij}^{(1)})^2 \right] \quad (6)$$

$$\geq -D_1 \delta + \frac{1}{3} D_2 \delta^2 \quad (7)$$

$$\approx -\delta_{\text{lin}} + \frac{1}{7} \delta_{\text{lin}}^2 \equiv \psi_{2\text{LPT,parab}}(\mathbf{q}), \quad (8)$$

in the last line using the above approximation for D_2 .

Fig. 1 shows the 2LPT mapping between ψ_i and ψ_f ($\nabla_{\mathbf{q}} \cdot \Psi$ at redshifts 49 and 0, respectively), as well as the log-density $\ln(1+\delta)$, for particles in a Λ CDM 256³-particle, 200 h^{-1} Mpc-box size N -body simulation, analyzed and discussed further below. The particles were advanced using the 2LPT algorithm as described by Scoccimarro (1998). In this standard technique, also used in producing a ZA realization, first a Gaussian random field ψ_i is generated. ψ_f is then estimated using an LPT approximation, and the final displacement field is generated in Fourier space with an inverse-divergence operator.

For the top panel, the divergence was measured in Fourier space, the native technique in the algorithm that produced the particle distribution,

$$(\nabla \cdot \psi)_k = -i\mathbf{k} \cdot \psi_k. \quad (9)$$

For the middle panel, and in the rest of this paper, $\psi(\mathbf{q})$ was measured in real space by differencing Eulerian positions of particles immediately before and after the particle at position \mathbf{q} , in Lagrangian rows and columns of the initial lattice along the three Cartesian directions.

There is a noticeable difference between the two methods of measuring ψ_f in the top panels. One reason for this is that the effective resolution of the real-space ψ_f estimator is twice that of the Fourier-space estimator.

Particularly using the Fourier-space estimator, the 2LPT prediction fails at high ψ . Naively equating ψ_f and $-\delta$, this predicts strong overdensities in initial underdense regions! This behavior is

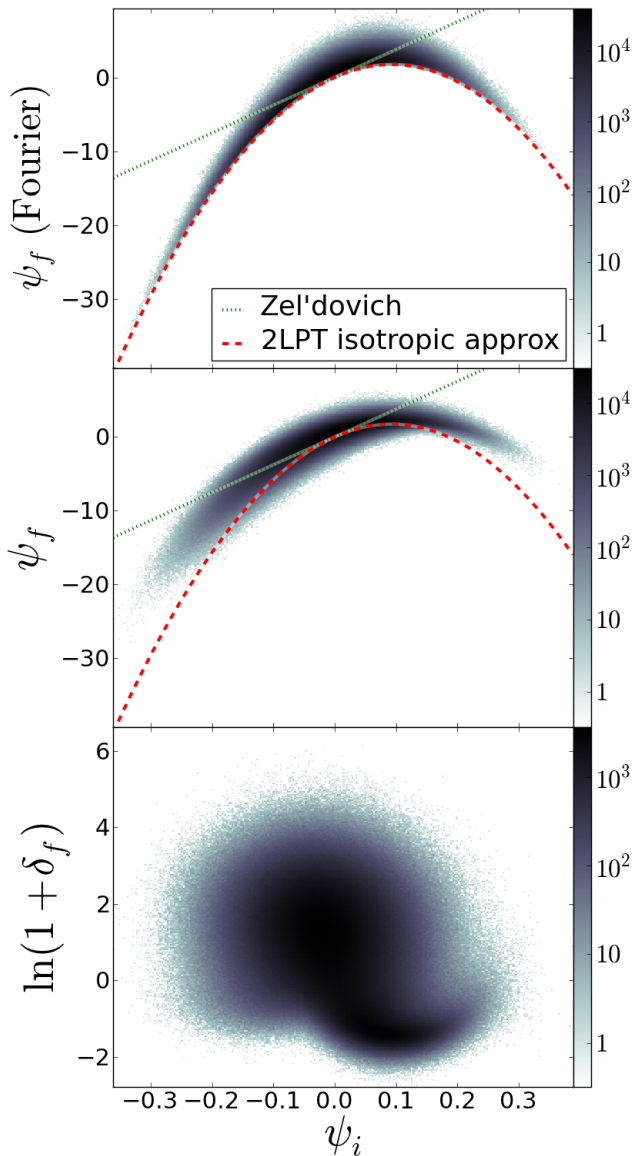


Figure 1. Two-dimensional histograms showing the relation between the stretching parameter $\psi(\mathbf{q}) = \nabla_{\mathbf{q}} \cdot \Psi(\mathbf{q})$, as well as the log-density, in the initial and final conditions, advancing particles according to second-order Lagrangian perturbation theory (2LPT). In the top panel, ψ is measured in Fourier space; in the middle, it is measured by differencing particle positions. The density in the bottom panel is estimated using a Voronoi tessellation, and is affected by multi-streaming. The color of each grid cell corresponds to the number of particles (out of 256^3) in that bin. In the top panels, dotted green lines show the linear relationship in the Zel'dovich approximation, and the dashed red curve shows the isotropic approximation $\psi_{2LPT, \text{parab}}$ of Eq. 8.

tempered in the real-space-estimated ψ_f , but still there are many apparently overdense, initially underdense particles.

This raises the question of whether artificial haloes might pop up in what should be voids using 2LPT. This is important since 2LPT is sometimes used to generate low-redshift density distributions, for example in modelling a sparsely sampled, large-volume survey, where only the clustering on large (e.g. baryon-acoustic-oscillation) scales needs to be accurate (e.g. Scoccimarro & Sheth 2002; Neyrinck & Szapudi 2008; Manera et al. 2012).

As one test of this issue, we show the density as well in Fig. 1, measured with a Voronoi tessellation (e.g., Schaap & van de Weygaert 2000; Neyrinck et al. 2005; van de Weygaert & Schaap 2009). For this Voronoi density estimate, each particle occupies a Voronoi cell, a locus of points closer to that particle than to any other particle. The overdensity $\delta_{VTFE} = \langle V \rangle / V - 1$ at a particle is set according to the volume V of its cell. This density measure is mass-weighted, and thus in a sense Lagrangian, but only strictly Lagrangian without multi-streaming, which does occur in this 2LPT realization.

In the bottom panel of Fig. 1, at moderate to high densities, there is little correlation between ψ_i and δ . The over-shell-crossing in LPT, evident below in Fig. 10, is one reason for this. At low densities, there are indeed a few overdense particles that have low ψ_i . We find this also below in Fig. 12, after which we further discuss this issue.

Previous authors (Buchert et al. 1994; Bouchet et al. 1995; Sahni & Shandarin 1996) have noted the failure of 2LPT in voids; they also found that going to third-order LPT (3LPT) does not improve agreement substantially. 3LPT comes at the expense of significantly greater complexity, and the addition of a nonzero curl component (as exists in full gravity, as well). Since we have adopted the approximation that the displacement field is potential in this paper, we stop our LPT analysis at second order.

2.2 The Spherical-Collapse Approximation

Bernardeau (1994b) gave a simple formula for the evolution of an average Lagrangian volume element, which gives a good fit to results based on the spherical-collapse (SC) model. It is based on an $\Omega_M \rightarrow 0$ (and $\Omega_\Lambda = 0$) limit he (Bernardeau 1992) found to the nonlinear spherical-collapse evolution of density. A concise, instructive derivation appears in (Bernardeau et al. 2002). Since the formula arises from a low-density limit, it is not surprising that it is quite accurate in voids in Λ CDM, so perhaps we should call it the spherical-expansion approximation. In this approximation, the mass element's volume, where V_0 is the mean volume occupied by a particle (assuming equal masses), is

$$V(t) = V_0 \left(1 - \frac{2}{3} \delta_{\text{lin}} \right)^{3/2}. \quad (10)$$

This approximation matches the behavior of ‘rare events’ (matter in deep voids) well. Fosalba & Gaztañaga (1998) discuss how this approximation arises, to leading order, in a monopole approximation to Lagrangian perturbation theory. This expression has proven to be quite accurate, even outside of the ‘rare-event’ limit in which it was originally proposed, over a wide range of regimes and cosmologies (Fosalba & Gaztañaga 1998). Scherrer & Gaztañaga (2001) found that including a full parametric description of spherical-collapse dynamics further improved matters, however at the expense of additional complication and computation.

To get an equation for the time evolution of ψ out of this, we use a geometric isotropic-cube approximation to relate δ and ψ . The below derivation also essentially appears in Mohayaee et al. (2006). Assuming a Lagrangian mass element occupies a cube of side length $\psi/3 + 1$ (giving $\nabla_{\mathbf{q}} \cdot \Psi = \psi$), the volume of such a cube in units of the mean volume is

$$V = 1/(1 + \delta) = (\psi/3 + 1)^3. \quad (11)$$

Equating the RHS of Eq. (11) to the volume in Eq. 10, and employing the ZA $\psi_{\text{lin}} = -\delta_{\text{lin}}$ gives what we call the spherical-collapse (SC) approximation.

$$\begin{aligned}\psi_{\text{sc}} &= 3 \left[\left(1 + \frac{2}{3} \psi_{\text{lin}} \right)^{1/2} - 1 \right] \\ &= \psi_{\text{lin}} - \frac{1}{6} \psi_{\text{lin}}^2 + \frac{1}{18} \psi_{\text{lin}}^3 + O(\psi_{\text{lin}}^4),\end{aligned}\quad (12)$$

where $\psi_{\text{lin}} = \frac{D_1(\tau)}{D_1(\tau_0)} \psi_0$ for some initial time τ_0 . This is one of a class of local approximations in which ψ_f at a given final redshift and position depends only on its linear value, ψ_{lin} . In higher-order LPT, ψ_f is generally nonlocal, depending on derivatives of ψ_{lin} , as well.

3 LOCAL LAGRANGIAN APPROXIMATIONS

To explore some general relationships between the ‘stretching parameter’ ψ and density variables, we further explore them in a simple class of toy ‘local Lagrangian’ models introduced by Protopogeros & Scherrer (1997, PS97). These models are parameterized by $1 < \alpha < 3$,

$$\delta_\alpha(\psi) = (1 + \psi/\alpha)^{-\alpha} - 1. \quad (13)$$

Here, ψ is the actual ψ of a volume element, not necessarily related to the linearly evolved ψ_{lin} .

It may help to think of α conceptually as the effective number of axes along which volume elements are expanding or contracting. The cubic-mass-element approximation in Eq. (11) has $\alpha = 3$. However, confusingly, the $\alpha = 3$ relationship was used in deriving the $\alpha = 3/2$ SC approximation. α turns from 3 to 3/2 only when we add the spherical-collapse relationship of Eq. (10), which relates (‘final’) ψ to the linearly evolved ψ_{lin} .

The $\alpha = 3/2$ model is particularly useful, but α may take other effective values in other environments. So, we do not confine our attention exclusively to $\alpha = 3/2$.

In these models, density singularities arise at $\psi = -\alpha$, where the volume element has contracted to zero. In the SC approximation the critical density of a collapsed element is $-\psi_{\text{lin}} = 1.5$, close to the Einstein-de Sitter linear spherical-collapse density, 1.69.

One way to quantify the non-linearity of the ψ - δ relationship is in its Taylor-series coefficients. Eq. 13 expands to

$$\delta_\alpha(\psi) = -\psi + \frac{1+\alpha}{2\alpha} \psi^2 - \frac{(1+\alpha)(2+\alpha)}{6\alpha^2} \psi^3 + O(\psi^4). \quad (14)$$

In this family of approximations, the log-density

$$A_\alpha(\psi) \equiv \ln(1 + \delta_\alpha) = -\alpha \ln(1 + \psi/\alpha) \quad (15)$$

has a much more linear relationship to ψ than δ does (recalling that $\alpha \geq 1$):

$$A_\alpha(\psi) = -\psi + \frac{1}{2\alpha} \psi^2 - \frac{1}{3\alpha^2} \psi^3 + O(\psi^4). \quad (16)$$

Curiously, the log-density is also closely related to the Eulerian divergence of the displacement field (Falck et al. 2012a), perhaps even more so than the Lagrangian divergence, as we investigate here

In the next section, we will see that the distribution of A given a Gaussian-distributed ψ is also significantly more Gaussian than δ .

At early epochs in the Zel’dovich approximation, a cubic-mass-element model with $\alpha = 3$ describes the density distribution quite well. Fig. 2 shows the accuracy of this cubic-mass-element relationship in a set of ZA-produced Λ CDM initial conditions

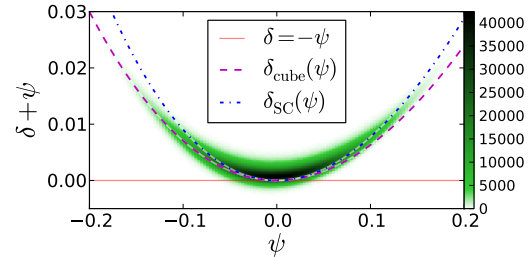


Figure 2. In green and black, two-dimensional histograms showing the relation between $\psi(\mathbf{q}) = \nabla_{\mathbf{q}} \cdot \Psi(\mathbf{q})$, and δ , for 256^3 particles in a set of $z = 49$ initial conditions produced using the Zel’dovich approximation (ZA). The deviation from $\psi = -\delta$ follows the cubic-mass-element approximation δ_{cube} for $\psi < 0$; for $\psi > 0$, the result is between δ_{cube} and δ_{SC} . The histogram is unnormalized, showing the number of particles in each bin.

at redshift $z = 49$. This simulation, used below, has 256^3 particles, and box size $200 h^{-1}$ Mpc. Again, the density was estimated with a Voronoi method at each particle; here, it is a true Lagrangian density estimate, since the fluctuations are small enough that no multi-streaming has occurred.

Although the nonlinearity in Fig. 2 is a bit accentuated by the stretched y -axis, it is still substantial. Putting $\alpha = 3$ in Eqs. (14) and (16), the ψ^2 coefficients in δ and A are $2/3$ (rather large; by far the highest among the approximations here explored) and $1/6$.

3.1 Density PDFs

Analytical density PDFs easily emerge from such local Lagrangian approximations, which consist of simple transformations on initial distributions. Here we assume a Gaussian distribution in ψ , but a non-Gaussian ψ could also be transformed.

Note that even without explicit initial non-Gaussianity at arbitrarily early times, a Gaussian distribution in ψ results in a non-Gaussian δ distribution. If a Gaussian δ distribution is truly desired, one could start with an appropriately non-Gaussian ψ distribution, though we do not explore this possibility here.

We transform the distributions with the change-of-variables formula

$$P(y) = P(x) |dx/dy|, \quad (17)$$

where $P(x)dx$ and $P(y)dy$ give the PDFs of variables x and y .

PS97 worked out the PDF of δ for the above α -parameterized local-Lagrangian approximations, allowing shell crossing by using the absolute value of the volume element in Eq. (13). Here, we take a slightly different approach, removing volume elements that have undergone shell crossing (i.e. with $1 + \psi/\alpha < 0$) from consideration. This leads to a PDF that does not integrate entirely to 1, although its integral is bounded below by 1/2 for large σ_ψ , and differs negligibly from 1 for $\sigma_\psi \lesssim 0.5$. Assuming the fraction of such removed particles is small, i.e. for $\sigma_\psi \lesssim 0.5$, the PDF of δ_{Lag} , the mass-weighted density distribution, is

$$P(\delta_{\text{Lag}}) = \frac{\exp \left[-\alpha^2 \left\{ (1 + \delta)^{-1/\alpha} - 1 \right\}^2 / (2\sigma_\psi^2) \right]}{(1 + \delta_{\text{Lag}})^{-1-1/\alpha} \sqrt{2\pi\sigma_\psi^2}} \quad (18)$$

An Eulerian PDF for δ can be obtained by multiplying the Lagrangian PDF by a factor of $V/\langle V \rangle$, where $V = 1/(1 + \delta)$, giving

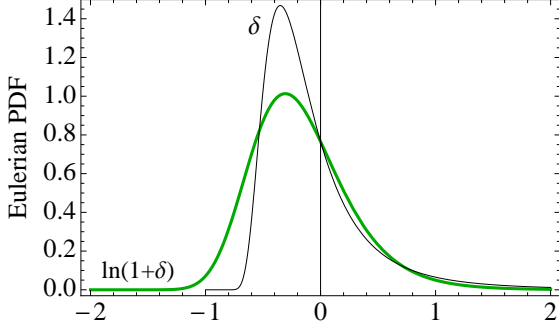


Figure 3. Eulerian PDFs of δ and $A = \ln(1 + \delta)$ from Eqs. (19) and (21), setting $\alpha = 3/2$ and $\sigma_\psi = 0.5$.

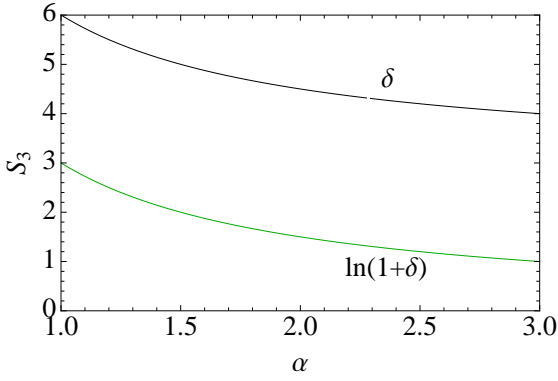


Figure 4. Skewness parameters S_3 , for both the overdensity δ and the log-density A , letting $\sigma_\psi \rightarrow 0$, as a function of α , using Eqs. (19) and (21). The curves are computed numerically, but match the relations in Eq. (22).

$$P(\delta_{\text{Eul}}) = \frac{\exp\left[-\alpha^2 \left\{ (1 + \delta)^{-1/\alpha} - 1 \right\}^2 / (2\sigma_\psi^2)\right]}{(1 + \delta_{\text{Lag}})^{-2-1/\alpha} \left(1 + \frac{\alpha-1}{2\alpha} \sigma_\psi^2\right) \sqrt{2\pi\sigma_\psi^2}} \quad (19)$$

The middle factor in the denominator is $\langle V \rangle$, which we found to have the form $1 + V_2(\alpha)\sigma_\psi^2$ for $1 < \alpha < 3$. The form for V_2 gives the analytically calculable coefficient at $V_2(\alpha = 1, 2, 3) = (1, 1/4, 1/3)$, and matches the numerically estimated coefficient at other α 's, including the SC $V_2(3/2) = 1/6$.

3.2 Reduced non-Gaussianity in the log-density

As is well-known in cosmology (e.g., Coles & Jones 1991; Colombi 1994; Neyrinck et al. 2009), the PDF of the log-density, $A \equiv \ln(1 + \delta)$, is much more Gaussian than the PDF of δ . One way to understand this is that $P(\delta)$, unlike $P(A)$, is tied down to zero at $\delta = -1$. Because it is so easy to do in the α -parameterized model, here we give some explicit formulae for the PDF and skewness of A .

A Gaussian ψ distribution transforms to

$$P(A_{\text{Lag}}) = \frac{\exp\left[-\frac{A}{\alpha} - \frac{\alpha^2}{2\sigma_\psi^2} \left(e^{-A/\alpha} - 1\right)^2\right]}{\sqrt{2\pi\sigma_\psi^2}}. \quad (20)$$

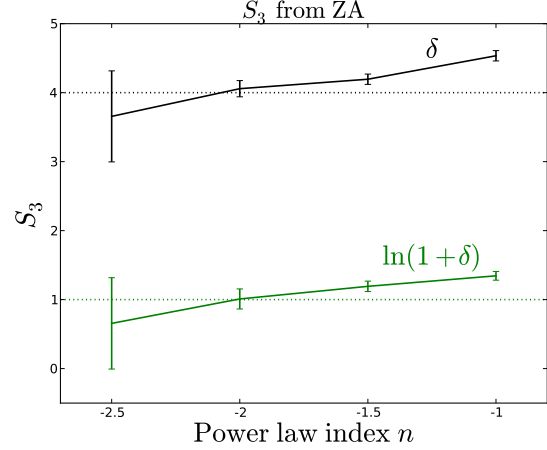


Figure 5. Volume-weighted skewnesses of A and δ , measured from Voronoi-cell volumes around particles in Zel'dovich realizations with power-law power spectra of indices n . The dotted curves are the asymptotic $\sigma_\psi \rightarrow 0$ values of S_3 in the cubic-mass-element model.

$$P(A_{\text{Eul}}) = \frac{\exp\left[-A\left(1 + \frac{1}{\alpha}\right) - \frac{\alpha^2}{2\sigma_\psi^2} \left(e^{-A/\alpha} - 1\right)^2\right]}{\left(1 + \frac{\alpha-1}{2\alpha} \sigma_\psi^2\right) \sqrt{2\pi\sigma_\psi^2}}, \quad (21)$$

with the same $\langle V \rangle$ factor in the denominator as in Eq. (19).

Fig. 3 shows Eulerian (volume-weighted) PDFs of δ and A using the SC $\alpha = 3/2$, with $\sigma_\psi = 0.5$. Even at this modest σ_ψ , A is visibly more Gaussian than δ .

The first-order non-Gaussianity statistic is the skewness $S_3 = \langle \delta^3 \rangle / \langle \delta^2 \rangle^2$, which has been worked out perturbatively in the mildly non-linear regime, in both Eulerian perturbation theory (EPT) and in the Zel'dovich approximation. Without any smoothing, to Eulerian second ('tree') order, $S_3 = 34/7 \approx 4.86$ in an Einstein-de Sitter (EdS) universe (Peebles 1980), with small corrections in the Λ CDM case. In the Zel'dovich approximation, $S_3^{\text{Zel}} = 4$ (Bernardeau 1994a; Fry & Scherrer 1994), a bit lower. If the skewness measurement is done smoothing over equal-sized Eulerian cells, a term is added that depends on the (local) power-spectrum slope $n_{\text{eff}} = d \ln \sigma^2(R) / d \ln R$, where R is the smoothing radius. With smoothing, $\gamma = -(n_{\text{eff}} + 3)$ is added to S_3 .

In several cases, we found that S_3 in the limit of small fluctuations was reduced by 3 when measuring it from A instead of δ . The simplest example is the exact lognormal distribution, for which, analytically, the skewness of the log-density $S_3^A = 0$, and $S_3 = 3$, for any σ_A . A more general reduction of the skewness by 3 may only hold precisely in other cases in the limit $\sigma_\psi \rightarrow 0$.

Fig. 4 shows our numerical (using Mathematica) estimate of S_3 and S_3^A as a function of α , letting $\sigma_\psi \rightarrow 0$. The relations

$$S_3 = 3/\alpha + 3, \text{ and } S_3^A = 3/\alpha \quad (22)$$

match the numerical solution, as well as our and PS97's analytical findings (at $\alpha = 1, 3/2$, and 3). $S_3(\alpha = 3/2) = 5$ is close to the full-gravity value from EPT mentioned above, $34/7 \approx 4.86$, which is also the leading-order result in the full spherical-collapse model in the EdS case (Fosalba & Gaztañaga 1998; Bernardeau et al. 2002). In fact, $S_3 = 5$ in the limit $\Omega_\Lambda \rightarrow 0$ of the full SC dynamics. This match to the $\alpha = 3/2$ skewness is not surprising since the $\alpha = 3/2$ model arises in the same limit.

It may be worth investigating tuning the α parameter further, for example to investigate a model with $\alpha = 21/13 \approx 1.62$, which would exactly give the EdS EPT and SC skewness, and at the same time give a critical collapse $\psi_{\text{lin}} = -1.62$ for collapse, nearly the full nonlinear spherical-collapse value of $\psi_{\text{lin}} \approx -1.686$.

As PS97 found, in the cubic-mass-element approximation as $\sigma_\psi \rightarrow 0$, $S_3 = 4$ as in the ZA, although S_3 diverges from 4 differently than in the ZA as σ_ψ departs from 0. We numerically investigated S_3 in the ZA, measuring the volume-weighted particle-density skewness parameter S_3 from several ZA realizations. The Zel'dovich-produced Λ CDM initial conditions of the simulation shown in subsequent sections have $S_3 = 4.01$, and $S_3^A = 1.07$.

Fig. 5 shows the volume-averaged skewness in δ and A measured from the distribution of particle Voronoi densities in Zel'dovich simulations with power-law power spectra. The error bars are the dispersions among 3 realizations at each n . As n decreases, large-scale over small-scale fluctuations dominate. S_3 diverges somewhat from 4 at high n . In the context of the α model, it makes intuitive sense that the isotropic, cubic-mass-element would be most valid for low n , where large-scale fluctuations dominate. As n increases, mass elements cease to expand or contract isotropically, so the effective α decreases.

Note that this measurement, although it is Eulerian (volume-weighted), does not include a smoothing of the type that would add a γ term to S_3 , since there is no fixed cell size. Of course, the realizations have finite (mass) resolution; thus ‘no smoothing’ is not meant to imply infinite spatial and mass resolution. A γ term from a fixed Eulerian cell size would cause S_3 to depart from 4 in the opposite way than we observe when n is increased from -3 . The σ_ψ used to generate each realization was held fixed at 0.02, and the power-law index n was varied from -1 to -2.5 . Error bars show the dispersion from three different realizations analyzed at each n .

From these numerical results, it appears that in the ZA, as well as in the α approximation, a log transform reduces S_3 by 3. It would be interesting to show how widely this property holds, a question for later work.

4 BEHAVIOR OF ψ IN FULL GRAVITY

Here we compare these theoretical estimates to what actually occurs in an N -body simulation. The simulation has 256^3 particles in a $200\text{-}h^{-1}$ Mpc box, run with a vanilla Λ CDM cosmology ($\Omega_m = 0.3$, $\Omega_\Lambda = 0.7$, $\sigma_8 = 0.9$, $h = 0.73$, $n_s = 1$). The initial conditions were generated at redshift $z = 49$ using the Zel'dovich approximation, and run with the GADGET 2 (Springel 2005) code. The spatial stretching parameter $\psi(\mathbf{q}) \equiv \nabla_{\mathbf{q}} \cdot \Psi(\mathbf{q})$ is measured by numerically differencing neighboring particle positions.

Fig. 6 shows the evolution of $\psi(\mathbf{q})$ with redshift, showing 2D histograms of initial to final ψ at different snapshots. At moderate and low densities, the initially straight line at $z = 49$ grows bent, and develops a scatter (accentuated somewhat by the color scale). At high densities, there is a critical value $\psi = -3$, signifying collapse of the mass element. In an idealized case where a Lagrangian patch of particles contracts into a single point (a ‘halo’), $\psi = -3$. Here, the Lagrangian divergence of the particle-position field $\mathbf{x}(\mathbf{q})$ is zero; $\psi = \nabla_{\mathbf{q}} \cdot \mathbf{x} - 3 = -3$.

The locality of the ψ_f - ψ_i relationship can be measured with the dispersion in these 2D histograms. At $z = 0$, as expected, the locality is high in void regions, and degrades at higher densities, but, considering the stretched color scale, the relationship is still rather tight.

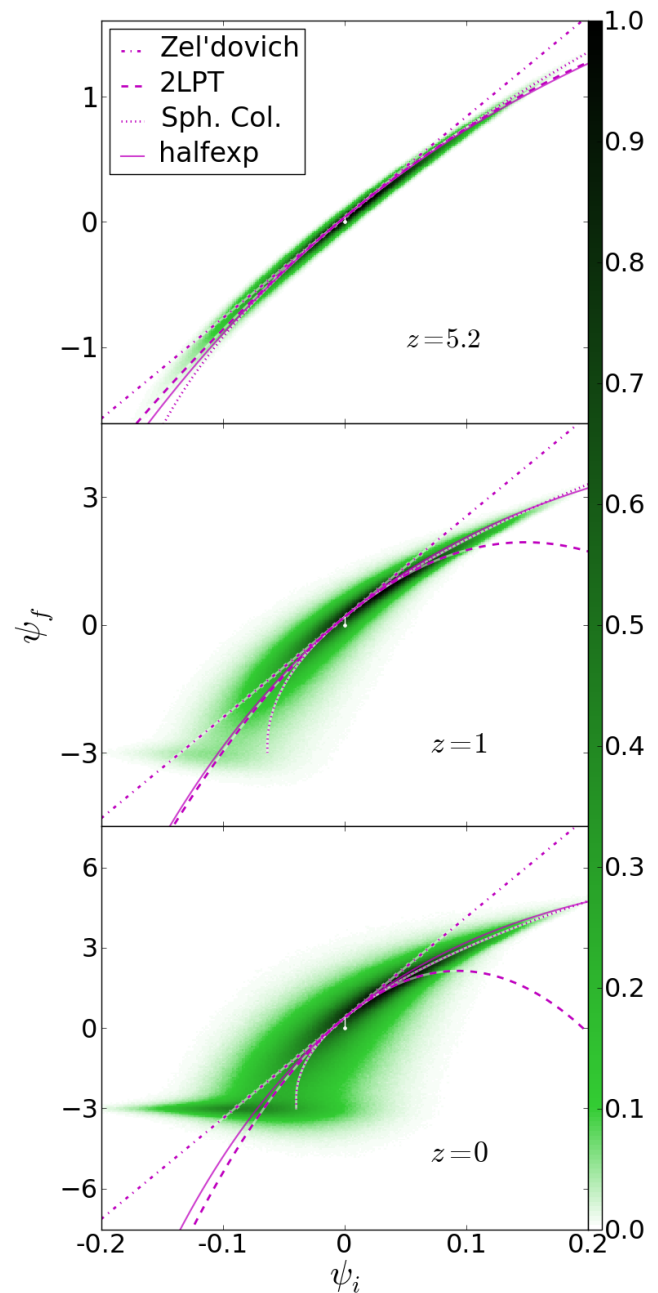


Figure 6. In green, two-dimensional histograms showing the relation between ψ_i at the initial redshift of 49, and ψ_f , measured at the redshifts listed. In a ‘local Lagrangian’ approximation, ψ_f is simply a function of ψ_i . With time, the dispersion between the two grows, but even at $z = 0$, the dispersion is rather low (considering the stretched color scale). Various local Lagrangian approximations are shown in magenta. The 2LPT curve, from Eq. 8, is a lower bound on $\psi_{2\text{LPT}}$. For a high-density mass element, ψ_f migrates downward until the element collapses, giving $\psi_f = -3$, about which it oscillates afterward. The small white circles and lines about (0,0) show the magnitude of the shift in the approximation curves caused by enforcing $\langle \psi_f \rangle = 0$.

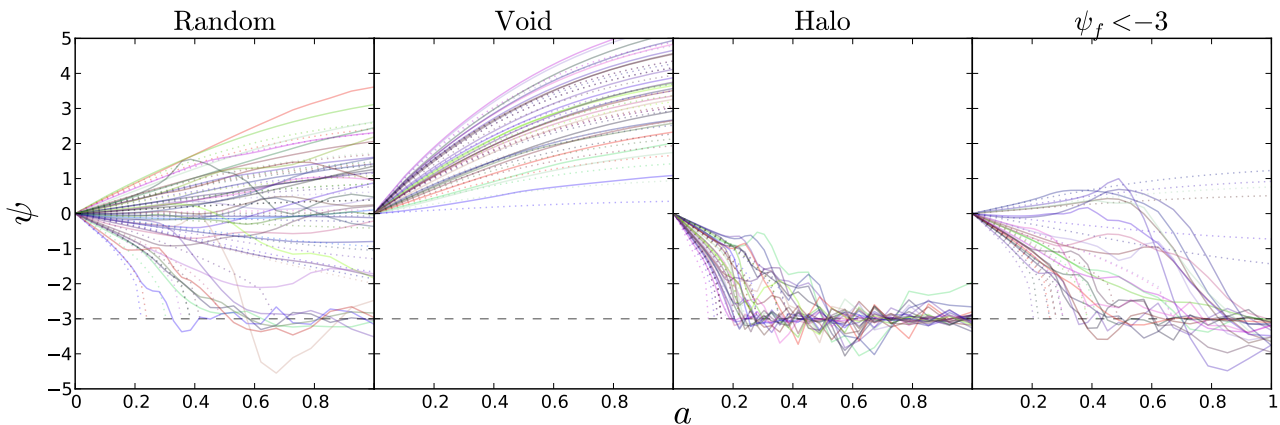


Figure 7. Trajectories in ψ , as a function of cosmic scale factor a , of four sets of particles, 25 in each panel, drawn from the two-dimensional slice shown below of an N -body simulation. From left to right: (1) A random set of particles; (2) particles within a Lagrangian distance of $2.3 h^{-1}$ Mpc of the maximum- ψ_i (lowest-initial-density) particle in the slice; (3) particles within a Lagrangian distance of $2.3 h^{-1}$ Mpc of the minimum- ψ_i (highest-initial-density) particle in the slice; (4) a random subset of particles with $\psi_f < -3$. Dotted curves show $\psi_{sc}(\psi_i)$, using Eq. (12), colored the same as each particle’s actual trajectory. The dashed line indicates the $\psi = -3$ collapse ‘barrier.’

As before, ψ was measured by differencing the positions of Lagrangian-neighbor particles. The development of the $\psi = -3$ peak in ψ_f is sensitive to the method of measuring ψ ; it does not appear if the divergence is measured in Fourier space. Perhaps this arises from sharp edges being difficult to describe precisely in Fourier space.

Once a particle crosses the $\psi = -3$ barrier, ψ changes stochastically, but stays around -3 , since Lagrangian neighbors stay nearby in a halo compared to the Lagrangian interparticle separation (assuming somewhat low mass resolution). Thus a collapsing mass element’s ψ value evolves as though it were in a waterfall: it descends with time as the mass element’s density increases, then hits a ‘surface’ at $\psi = -3$, about which it then bobs around.

For $\psi_i < 0$ but $\psi_f > -3$ (at high densities before actual collapse), the best of the above approximations for $\psi_f > -3$ seems to be $\psi_{2LPT,parab}$ (Eq. (8)), lying between the overpredicting Zel’dovich (Eq. (1)) and the underpredicting SC [Eq. (12)] predictions. For $\psi \geq 0$ (at low densities), the SC prediction is best, again lying between the two rather poor alternatives. Curiously, these two approximations are both parabolic, one in ψ_i , and the other in ψ_f .

We found empirically that another approximation shown,

$$\psi_{\text{halfexp}} = D^{1/2} \left(1 - e^{-D^{1/2} \psi_i} \right), \quad (23)$$

works well for both high and low ψ_i . However, we caution that to our knowledge it lacks theoretical motivation, and has strange behavior at very high ψ (higher than plotted here), asymptoting to $D^{1/2}$.

The curves do not precisely go through the origin, which appears as a white dot. The offsets, shown by small white lines, ensure that $\langle \psi_{sc} \rangle = 0$. For simplicity, we apply the same offset to all curves. The numerical value of this offset is similar for the various approximations, except for the ZA, for which ψ_f is always symmetric about zero. This $\langle \psi \rangle = 0$ condition ensures that there is no mean comoving expansion or contraction.

The SC approximation, ψ_{sc} , predicts a particular trajectory of ψ with time, depending only on the local ψ_{lin} . To investigate how well this approximation holds with time, for particles in different environments, in Fig. 7 we show trajectories in ψ for particles in

various classes: a random selection of particles; particles near the highest-initial-density and the lowest-initial-density particles; and particles with $\psi_f < -3$. At early epochs ($a \lesssim 0.2$), ψ tracks ψ_{sc} well. Subsequently, particles participating in nonlinear structures can get seriously derailed (e.g., the rightmost panel). Still, there are many particles for which ψ continues to track ψ_{sc} . In the deepest void, for example (second-left panel), the form of the expansion roughly tracks the SC prediction, but is skewed upward, perhaps due to the extremity of the void.

Fig. 8 shows ψ_f , measured at $z = 0$ for 256^2 particles occupying a flat Lagrangian sheet from this simulation. Some similar figures appear in Mohayaee et al. (2006). The quantities are plotted in Lagrangian (initial-conditions) coordinates, with each pixel corresponding to a particle on the square lattice. Also plotted are the ORIGAMI (Falck et al. 2012b) morphologies of the particles in the sheet, as well as the result of applying the spherical-collapse equation (12) to the initial conditions. A particle’s morphology in the ORIGAMI algorithm measures the number of Lagrangian axes along which other particles have crossed it in Eulerian space. A halo particle has been crossed by other particles along 3 orthogonal axes; filament, wall, and void particles have been crossed along 2, 1, and 0 orthogonal axes. In the bottom panels, if $\psi_{\text{lin}} < -3/2$, Eq. (12) has no solution, i.e. the mass element has collapsed; in this case, we set $\psi_{sc} = -3$. Contours indicate the boundaries of ORIGAMI halo regions.

The color scheme suggests a topographical analogy, when working in Lagrangian coordinates: as time passes, ψ departs from zero, in a way largely prescribed by its initial value. However, in overdense regions where it is decreasing, it is not allowed to plummet arbitrarily; where collapses occur, ‘lakes’ form, where ψ becomes ≈ -3 .

In the upper-right panel, the blue ‘lakes’ of ψ_f correspond quite well to halo regions as identified by ORIGAMI. A simple halo-finder comes to mind, connecting particles on the Lagrangian lattice with ψ under some threshold, approximately -3 . We did try a simple implementation of this, but had difficulty finding a simple threshold to characterize all haloes, since there are roughly as many halo particles with $\psi > -3$ as $\psi < -3$. Still, we suspect a halo-finder along these lines could be quite successful.

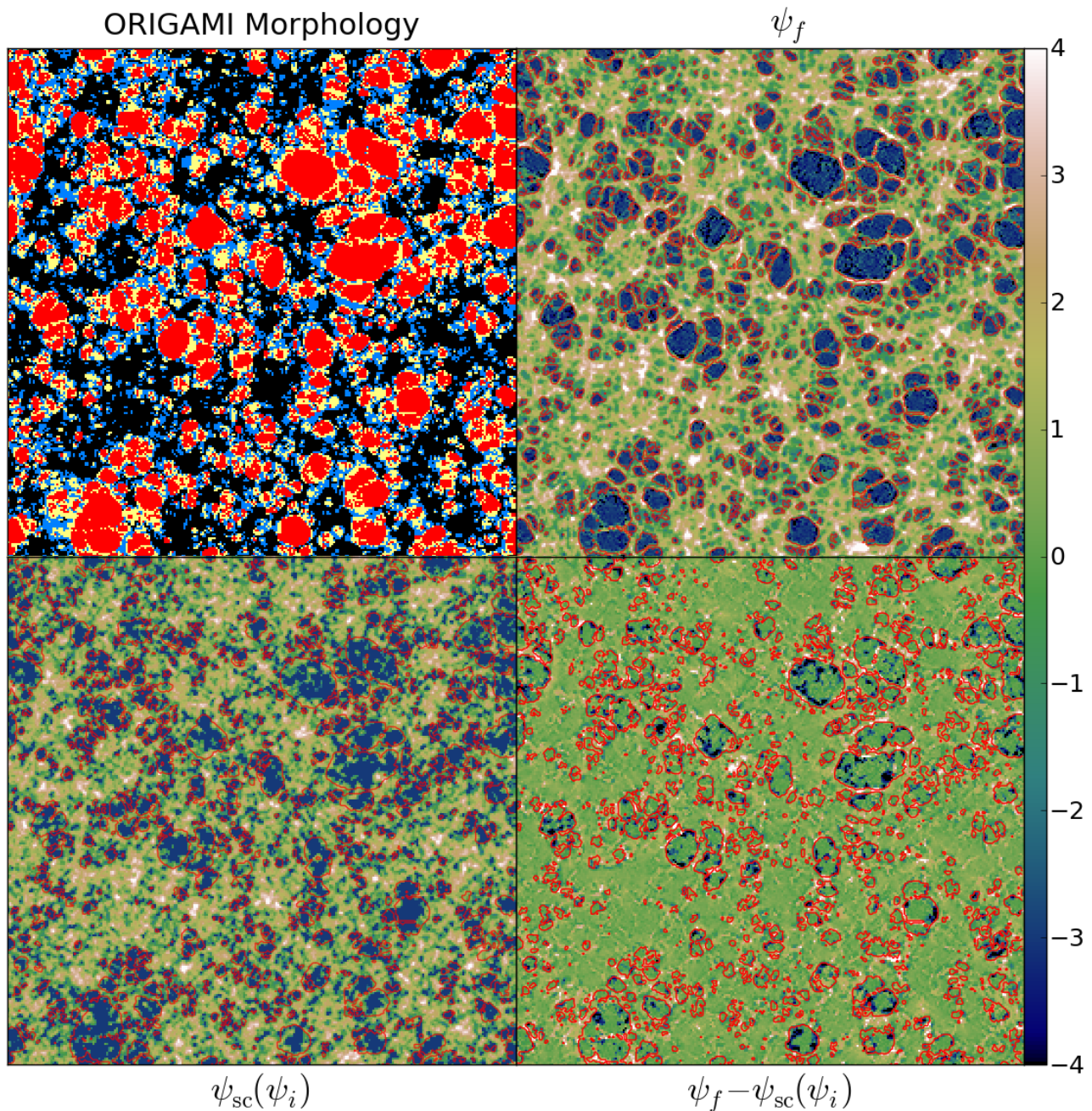


Figure 8. Quantities measured on a Lagrangian sheet of 256^2 particles from a 256^3 -particle simulation of box size $200 h^{-1}$ Mpc, run to redshift 0. Each pixel corresponds to a particle. Upper left: the ORIGAMI morphology of the particle (void, wall, filament and halo particles are colored black, blue, yellow and red). Upper right: the Lagrangian divergence of the displacement field, ψ_f . The ‘lakes’ are Lagrangian regions that have collapsed to form haloes. Lower left: a prediction from the initial-conditions ψ_i , using the spherical-collapse formula (12). ψ_f is set to -3 if $\psi_{\text{lin}} < -3/2$. Lower right: the difference between upper left and lower right. The red contours mark the boundaries of haloes as identified by ORIGAMI.

The bottom panels compare ψ_{sc} and ψ_f . As in Fig. 6, the two match quite well in void regions, but in high-density regions, the correspondence is rougher. The rms difference between ψ_{sc} and ψ_f in this simulation is 1.31. The agreement in overdense regions can be improved by using ψ_{sc} for $\psi > 0$, but $\psi_{2\text{LPT,parab}}$ for $\psi < 0$. This reduces the rms difference to 1.24. These are to be compared to the standard deviation of ψ_f (i.e. the rms if it is approximated with its mean, 0), which is 2.0.

Another interesting feature of this plot is that $\psi_f - \psi_{\text{sc}}(\psi_i)$ often plummets (i.e. becomes large and negative) on the Lagrangian outskirts of haloes. There are a couple of possible reasons for this. The particles have been dragged into the halo at late times, and may not be overdense initially. Also, as they have just fallen into haloes, their cubic Lagrangian volumes have likely just been swapped. Thus when a particle first collapses, ψ generally overshoots -3 , as also shown in Fig. 7.

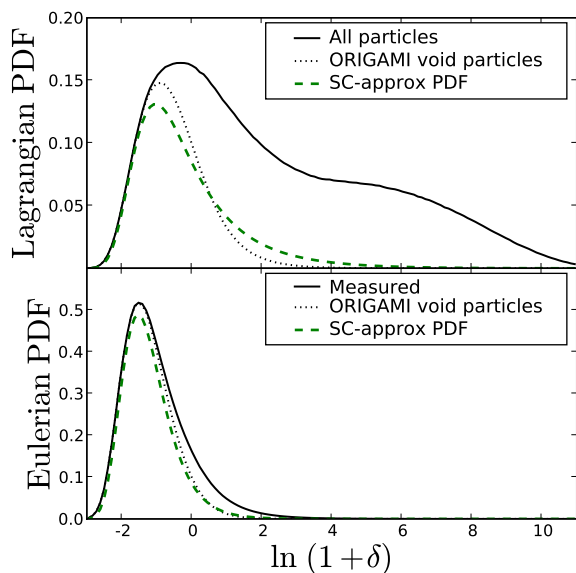


Figure 9. Voronoi-measured histograms of $A = \ln(1 + \delta)$, including all particles, and also including only ORIGAMI-identified void particles, which have undergone no stream-crossing. The theoretical PDFs are as in Eqs. (20) and (21), applying a normalization correction equal to the fraction of ORIGAMI void particles in the simulation. The top histogram is ‘Lagrangian’ as in mass-weighted, with each particle contributing equally. The bottom, Eulerian histograms are also measured using the Voronoi tessellation; they are simply the ‘Lagrangian’ PDFs multiplied by $V = 1/(1 + \delta)$.

Fig. 9 compares Voronoi-measured, mass-weighted PDFs to those assuming that each volume element evolves independently, i.e. the PDFs of Eqs. (18-21). Again, the ‘Lagrangian’ PDF is not truly Lagrangian, since the density estimate for a particle includes all other particles, not just its Lagrangian neighbors. Thus stream-crossing boosts each particle’s density according to the locally overlapping number of streams, populating the high-density ‘shelf’ that poorly matches the approximation.

At low densities, the approximations match the measurements well. PS97 also found this, albeit in simulations without as much structure. However, a normalization correction was necessary for the agreement in Fig. 9. A greater fraction of particles than predicted by the SC approximation leave the SC tracks to populate the high-density tail, as in Fig. 7.

If the SC approximation were precisely accurate in describing both the density evolution up to stream crossing, and the fraction of particles whose Lagrangian volumes have collapsed, no normalization correction would be necessary in Eq. (20), since as noted earlier, we did not divide by the integral over the PDF to assure a PDF integrating to unity. At this value of σ_ψ , Eq. (20) integrates to 0.71, which can be calculated with a simple Erf expression giving the fraction of particles with $(1 + \frac{2}{3}\psi_{\text{lin}}) < 0$ (the critical $-\psi_{\text{lin}} = 1.5$, intriguingly near the critical density for collapse, 1.69).

Instead, we found that a smaller factor, 0.34, gave a good fit to the low-density tail. This matches the fraction of void particles in this simulation snapshot as measured by the ORIGAMI (Falck et al. 2012b) algorithm. An ORIGAMI void particle has not been crossed by any other particle over the course of the simulation. We also show a curve showing the PDF of only void particles. The shape of this curve does not quite match that from the SC-approximation

PDF; that is, even higher-density void particles are scattered a bit to higher densities.

The agreement between all curves looks much better in the bottom, Eulerian panel. This is because the PDF is simply the PDF in the upper panel multiplied by the volume factor $V/\langle V \rangle$. In terms of the x -coordinate A , this is simply an exponential damping, e^{-A} , bringing up the left side of the curve, and suppressing the right side.

If the amplitude of this normalization correction can be estimated or calibrated accurately, Eqs. (20-21) seem to provide a convenient estimate for the nonlinear density PDF, if a PDF lacking the true, more-populated high-density tail is adequate.

5 PARTICLE REALIZATIONS FROM THE SC APPROXIMATION

Given that ψ_{sc} tracks the evolution of ψ well, we explored how well it would work explicitly to advance ψ_i to ψ_f using Eq. (12), additionally setting $\psi_f = -3$ for collapsed particles where $\psi_{\text{lin}} < -1.5$ (the singularity in Eq. (12)). This is a simple replacement for a ψ_i - ψ_f relationship in a Zel’dovich code, entailing only a fast additional step (with a bit less computational effort than 2LPT). This may be about as well as one can do with a local prescription giving ψ_f as a function of ψ_{lin} , with no dependence on its derivatives. (For comparison to a 2LPT prescription, see Appendix D2 of Scoccimarro (1998)). Here are all of the steps in our SC procedure:

- (i) Generate a Gaussian random field from a linear power spectrum. This becomes ψ_{lin} .
- (ii) For $\psi_{\text{lin}} \leq -1.5$, set $\psi_f = -3$. For $\psi_f > 1.5$, set $\psi_f = \psi_{\text{sc}} + C$, where ψ_{sc} is from Eq. (12), and C is a constant ensuring that $\langle \psi_f \rangle = 0$ (easily measurable by summing up ψ_f with $C = 0$). C is typically small; for example, in Fig. 6, C is the length of the small white line attached to the white dot.
- (iii) Take the inverse divergence of ψ_f (in Fourier space, inverting Eq. (9)) to get the displacement field Ψ .

Fig. 10 shows the particle positions resulting from advancing the initial ($z = 49$) conditions of this simulation to $z = 0$, compared to its actual $z = 0$ particle positions. The SC approximation gives a particle arrangement more visually similar to that using full N -body dynamics than using either of the LPT relations, for example producing more concentrated ‘haloes’ where $\psi = -3$. Still, they are not as pointlike as we had hoped, perhaps related to the difficulty of capture sharp edges in Fourier space. For example, measuring the divergence in Fourier space does not capture the $\psi_f = -3$ peak in Fig. 6. A completely real-space inverse-divergence algorithm might be more adept at producing tight haloes, but it is not obvious how such an algorithm would work.

Fig. 11 shows mass-weighted 1-point PDFs of each particle distribution. Here, the SC approximation gives the best approximation to the true dynamics, especially for the lowest densities, where the agreement is also quite good in Fig. 6. There is a ‘shelf’ of high-density particles; these correspond to particles in haloes. At higher resolution, this locus becomes a peak (Falck et al. 2012b). The low-density peak in the 2LPT PDF is a sign of its inaccuracy at this rather high ψ_{lin} dispersion, $\sigma(\psi_{\text{lin}}) = 2.7$.

Fig. 12 shows the same information in two-dimensional histograms, comparing the full-gravity (N -body) δ to δ in the approximately evolved realizations. Here, again ψ_{sc} performs best. In the low density region of the 2LPT scatter plot, there are in fact over-density particles (reaching at maximum $\delta \approx 8$), which should be

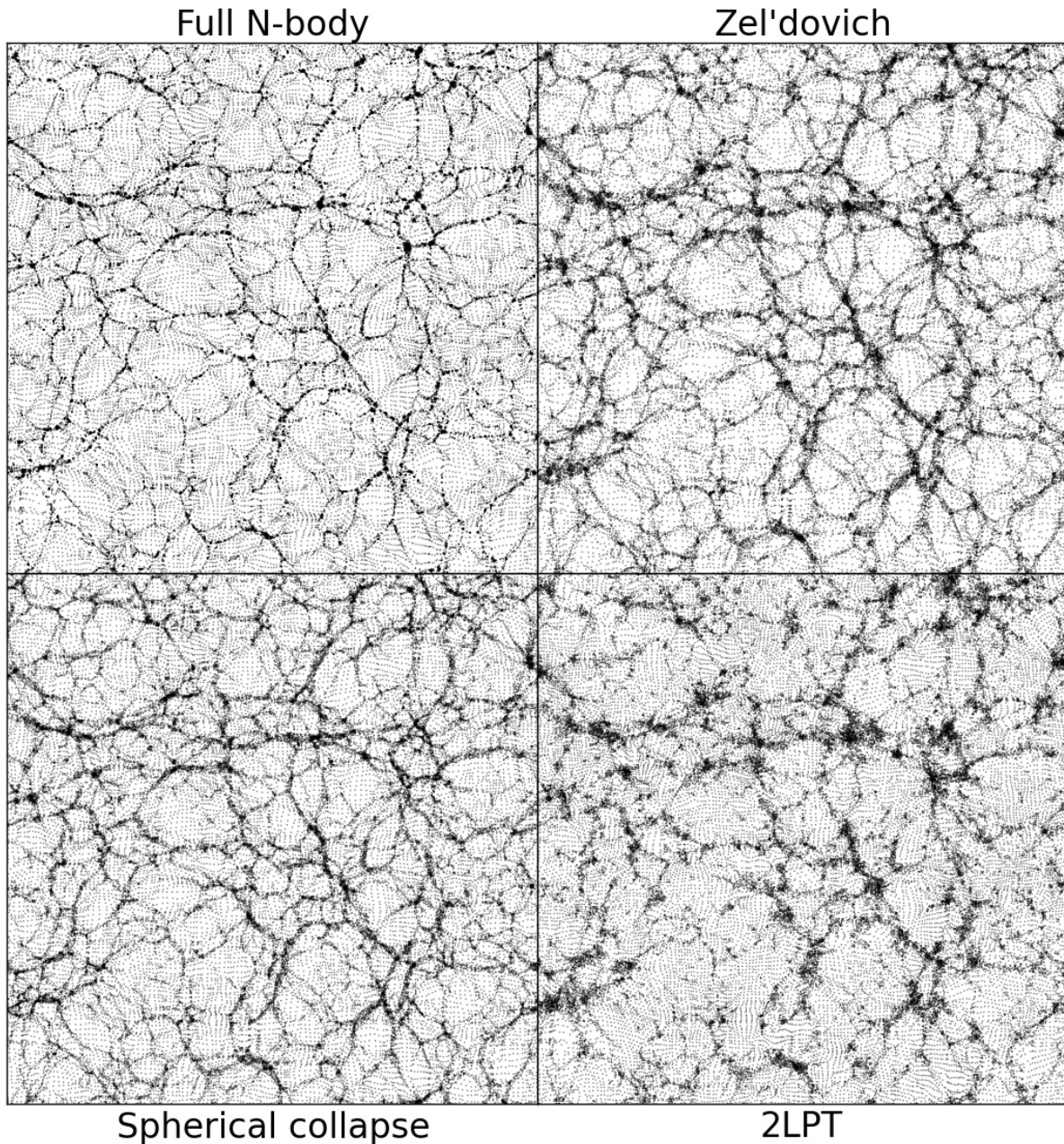


Figure 10. Redshift-zero Eulerian locations of particles occupying a 256^2 sheet of a 256^3 -particle Λ CDM realization, projecting out the third dimension. Clockwise from upper left, particle positions are determined using: a full N -body simulation; the Zel'dovich approximation; 2LPT; and the SC approximation (12). By eye, the SC approximation gives the results closest to full gravity.

extremely underdense in the final conditions. These middling overdensities are unlikely to produce spurious haloes detected in a 2LPT realization, but there remains some chance of that.

What are we to conclude about the reliability of 2LPT at low redshifts for mock galaxy catalogs? The work here is hardly an exhaustive study, as it considers just the single simulation analyzed here. But for this simulation at $z = 0$, the population of overdense particles that should be underdense starts to be a worry. This problem would be even more severe if $\sigma(\psi_{\text{lin}})$ were increased, populating the high- ψ_i branch of the $\psi_{2\text{LPT,parab}}$ parabola. One way to increase $\sigma(\psi_{\text{lin}})$ is by increasing the mass resolution (since fluctu-

ations grow on small scales in a Λ CDM universe), so we recommend caution in using 2LPT realization at high resolution and low redshift. This is not surprising, of course; for high LPT accuracy, $\sigma(\psi_{\text{lin}})$ should be $\lesssim 1$. Fortunately, to our knowledge, low-redshift uses of 2LPT have been at lower mass resolution than this, resulting in an appropriately low $\sigma(\psi_{\text{lin}})$.

While the SC approximation excels at predicting 1-point statistics and a visually plausible particle distribution, unfortunately it seems to have deficiencies, as well. The SC approximation shifts the locations of nonlinear structures more than does the ZA. This is difficult to see in Fig. 10, so we overplot the N -body and

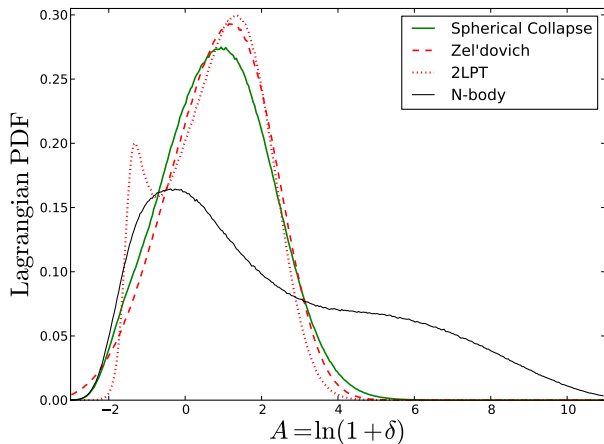


Figure 11. Mass-weighted histograms of Voronoi-estimated particle densities, for both the fully evolved initial conditions, and the three particle realizations shown in Fig. 10. The SC approximation performs best at low densities; all approximations fail to capture the second peak or shelf of high-density halo particles present in the full simulation. 2LPT even produces a PDF peak at low densities.

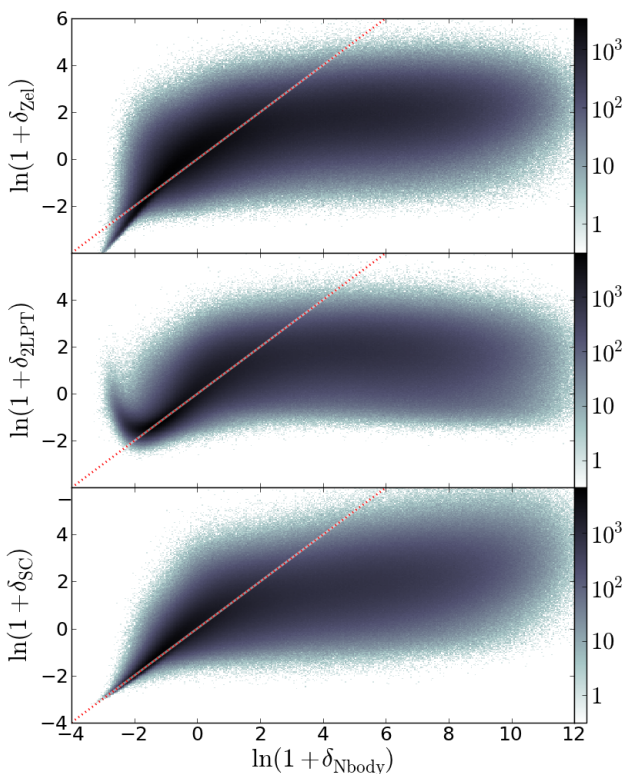


Figure 12. Two-dimensional histograms comparing particle densities evolved with full gravity (the x -axis) to densities in the approximately evolved particle distributions. The dotted red lines show the ideal $y = x$ locus. The SC-approximation-evolved particle distribution performs best. Note the turn-up at low densities in 2LPT, where some overdense particles are predicted among particles that should be in the deepest voids.

approximate realizations in Fig. 13. In 2LPT, structures have similar locations as in the ZA. We suspect that the discrepancy in the SC case is largely from voids that collapse in the full N -body case. In the LPT approximations, overdense structures surrounding the doomed voids collapse as they should, but this is suppressed in the SC case.

The differences in large-scale flows in the SC show up in root-mean-square errors in particle positions. The rms errors of particle positions compared to the full N -body dynamics using the three approximations are, respectively for Zel'dovich, 2LPT, and SC, 1.61, 1.65, and $2.17 h^{-1}$ Mpc.

The LPT approaches are also more successful than the SC approximation in predicting the low-redshift dark-matter power spectrum amplitude on large scales, as shown in Fig. 14. The power spectrum of particles displaced according to the SC approximation gives a multiplicative bias on large scales of about 0.65 in this simulation, although the SC power spectrum's shape is a bit closer to the shape of the full nonlinear power spectrum, turning down at smaller scales than do the LPT power spectra.

To measure the power spectra in Fig. 14, particles were displaced according to each approximation, and then assigned to cells on a 256^3 mesh using Nearest Grid Point mass assignment. Power spectra were then measured from these meshes, correcting for shot noise.

It is possible to fix this large-scale normalization issue by multiplying ψ_{lin} by a factor in Eq. (12). In Fig. 14, scaling ψ_{lin} by an extra factor of 2.0 achieves this. The factor was found by iteratively changing the effective growth factor until the power spectra agreed on large scales. This ‘corrected’ approximation also improves the agreement between the SC and N -body-evolved particles, bringing the rms error in particle positions down to $1.65 h^{-1}$ Mpc, at the level of the LPT approximations. However, undesirably, the ‘correction’ also reduces the SC power spectrum at small scales.

In Fig. 15, we show the Fourier-space cross-correlation coefficient $R(k) = P_{\delta \times \delta'} / \sqrt{P_{\delta} P_{\delta'}}$ between the $z = 0$ density field in this N -body simulation, and several other density fields. The ‘initial conditions’ curve is essentially the propagator (e.g. Crocce & Scoccimarro 2006). As pointed out recently by Tashev & Zaldarriaga (2012), the cross-correlation between Zel'dovich and full gravitational dynamics is significantly higher at small k than the cross-correlation between Eulerian linear PT and the full dynamics. The agreement is even a bit better in 2LPT. The SC realization has poorer performance here, on the other hand, although with the bias correction, $R(k)$ is the highest among the approximations at large k .

Other ideas we tried in obtaining ψ_f locally from ψ_i were to use ψ_{sc} for $\psi_i > 0$, but $\psi_{2\text{LPT,parab}}$ for $\psi_i < 0$, and also using ψ_{halfexp} , based on the agreement in both cases to the data in Fig. 6. These results were quite similar to the simple ψ_{sc} approximation, though.

It is quite likely that we could find some tweaking of these approximations that would empirically give the best results. However, we did not explore this avenue exhaustively, since this best agreement could be limited to this single simulation. Still, it seems likely that further optimization of the $\psi_i \rightarrow \psi_f$ mapping would be fruitful.

6 SUMMARY AND CONCLUSION

In this paper, we examine ψ , the Lagrangian divergence of the displacement field, arguably the most natural variable to quantify

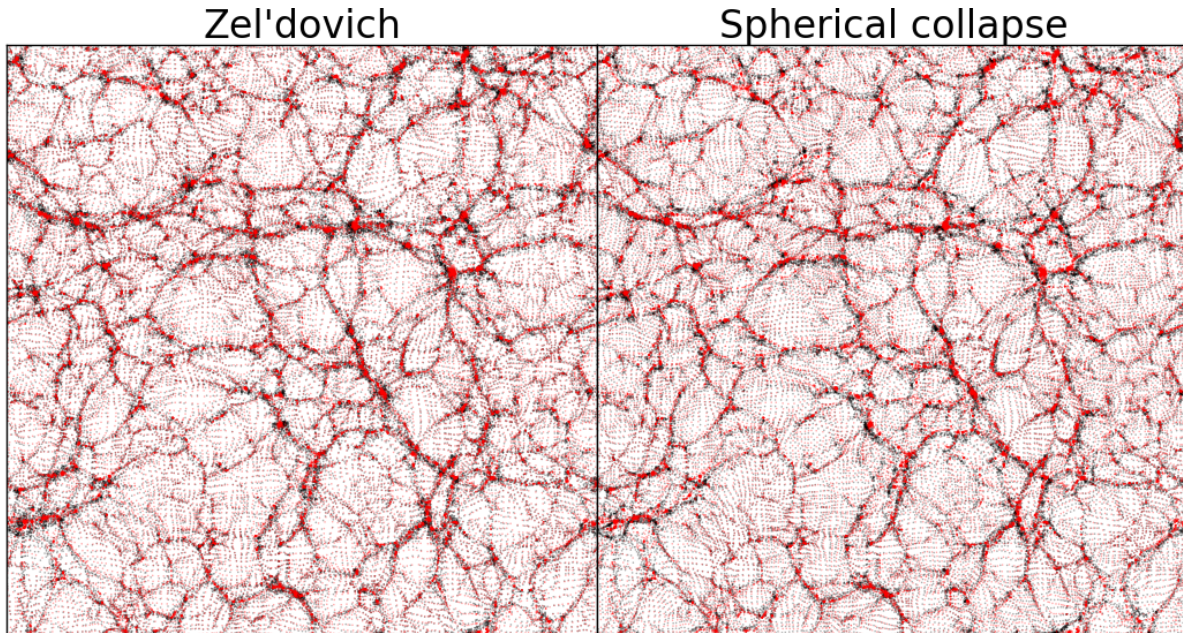


Figure 13. The Zel'dovich and SC panels of Fig. 10, with the full N -body results overlaid in red. While Zel'dovich gives artificially empty voids and fuzzier haloes, it gives somewhat more accurate large-scale flows than does SC.

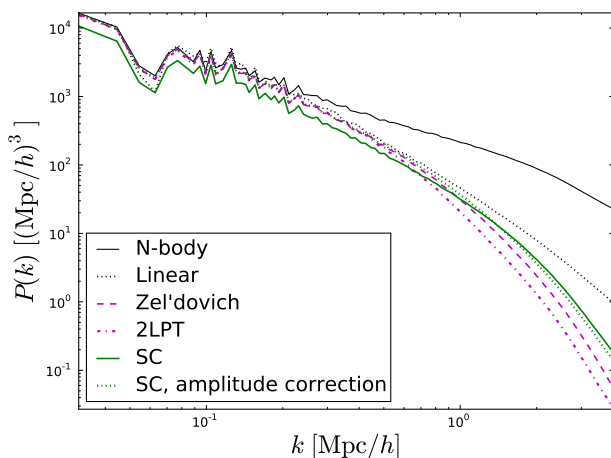


Figure 14. Matter power spectra in a $200-h^{-1}$ Mpc N -body simulation at $z = 0$, compared to power spectra of particle distributions displaced according to various approximations.

large-scale structure in a Lagrangian approach. The main results of the paper are as follows:

- Even slight distortions of the initially uniform mesh of particles, quantified by ψ , produce a density distribution more log-normal than Gaussian. It seems that for a wide class of models, the skewness parameter S_3 of the log-density field is reduced by 3 compared to the skewness of the overdensity.
- In 2LPT, the mapping from initial to final ψ is roughly parabolic, allowing overdensities to form where there should be deep voids. This does not seem to be a significant worry for a moderately low-density redshift-zero 2LPT realization ($\lesssim 1$ particle per $(h^{-1} \text{Mpc})^3$), but caution is recommended at higher resolution.
- The spherical-collapse-fit formula (12) describes the evolution

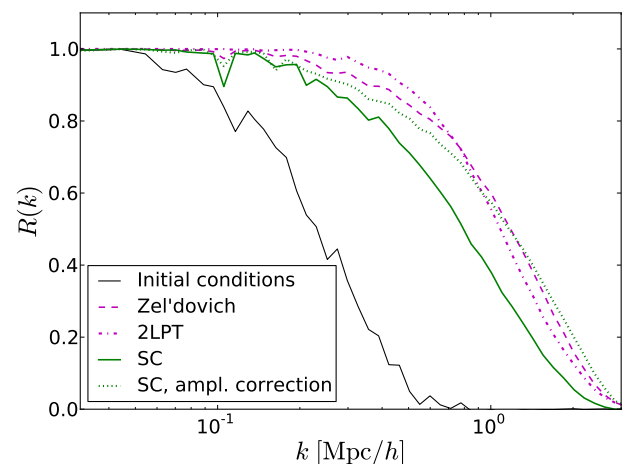


Figure 15. Fourier-space cross-correlation coefficients between the various approximately-evolved density fields and the particle distribution as evolved in the full N -body simulation. The solid black line is essentially the non-linear propagator between the initial and final states; the Lagrangian cross-correlations are higher, indicating higher accuracy.

of ψ from initial conditions better than first- or second-order Lagrangian perturbation theory (LPT), up to halo formation. This also allows for an approximation to the 1-point PDF of the density that works quite well for low-density, undisturbed (void) particles.

- In LPT, ψ gets arbitrarily small, indicating extreme stream crossing. In full gravity, however ψ gets stuck around -3 , signalling halo formation. This is the value it would have if Lagrangian regions contracted exactly to pointlike haloes.

• This knowledge of how ψ evolves allows for a new method to produce final-conditions particle positions, based on this SC expression. Compared to LPT realizations, such SC realizations give reduced stream-crossing, and better visual and 1-point-PDF corre-

spondence to the results of full gravity. LPT realizations, on the other hand, give more accurate large-scale flows and large-scale power spectra, as well as improved cross-correlation to the density field evolved with full gravity. An empirical correction may be added to the SC formula that seems to fix some of these issues, however.

Our results suggest several possibilities for future work. We did not carefully investigate the new SC method of generating final-conditions particle positions with respect to redshift and resolution. We suspect that the SC method could provide a good method of producing relatively low-redshift initial conditions for simulations, if such a thing is desired. It is true that the large-scale power-spectrum bias in this method is troubling, as are the shifts in large-scale flows, but these could be tied to $\psi = -3$ collapses, and could be absent at high redshift without stream-crossing.

The ‘barrier’ at $\psi = -3$ could be useful for halo-finding in N -body simulations. Unfortunately, it seems not straightforward to use this barrier to halo-find in a single snapshot of a simulation, but other possibilities exist. For instance, ψ could be measured at each timestep; if a particle ever has $\psi \leq -3$, it could be tagged as a halo particle.

It is also quite interesting to consider ways of predicting where $\psi = -3$ from the initial conditions. Such considerations may even allow provide analytical mass functions. Indeed, similar ideas have been proposed using LPT (e.g. Monaco et al. 2002). Another possible approach may be to infer Lagrangian halo boundaries from $\psi_{sc}(\psi_{lim})$ formula, as in the lower-left panel of Fig. 8. The true halo contours are often smoothed versions of these contours, and perhaps could be obtained by a combination of mathematical morphology techniques such as dilation and erosion (e.g. Serra 1983) in Lagrangian space, as can be useful in cleaning detected void boundaries (Platen et al. 2007).

In conclusion, ψ , a natural density-like variable in a Lagrangian viewpoint, seems to be a rather useful quantity, with some extra information that is not in the density itself. It is fortunate that a simple formula gives ψ 's behavior in voids, where dark energy is most energetically dominant (if indeed it is a substance). To understand dark energy, understanding the stretching of the Lagrangian mesh in voids is likely particularly important.

ACKNOWLEDGMENTS

I thank Guilhem Lavaux, Xin Wang, Alex Szalay, István Szapudi, Miguel Aragón-Calvo, Donghui Jeong and Nuala McCullagh for many helpful discussions; Miguel Aragón-Calvo additionally for use of the simulation analyzed here; and an anonymous referee for a helpful report. I am grateful for financial support from the Gordon and Betty Moore foundation and NSF award OIA-1124403.

REFERENCES

Abel, T., Hahn, O., & Kaehler, R. 2011, MNRAS, submitted, 1111.3944
 Arnold, V. 2001, Singularities of Caustics and Wave Fronts, Mathematics and Its Applications (Springer)
 Arnold, V. I., Shandarin, S. F., & Zeldovich, I. B. 1982, Geophysical and Astrophysical Fluid Dynamics, 20, 111
 Bernardeau, F. 1992, ApJ, 392, 1
 ——. 1994a, ApJ, 433, 1, arXiv:astro-ph/9312026
 ——. 1994b, ApJ, 427, 51, arXiv:astro-ph/9311066

Bernardeau, F., Colombi, S., Gaztañaga, E., & Scoccimarro, R. 2002, Phys. Reports, 367, 1, arXiv:astro-ph/0112551
 Bouchet, F. R., Colombi, S., Hivon, E., & Juszkiewicz, R. 1995, A&A, 296, 575, arXiv:astro-ph/9406013
 Buchert, T., Melott, A. L., & Weiss, A. G. 1994, A&A, 288, 349, arXiv:astro-ph/9309056
 Coles, P., & Jones, B. 1991, MNRAS, 248, 1
 Coles, P., Melott, A. L., & Shandarin, S. F. 1993, MNRAS, 260, 765
 Colombi, S. 1994, ApJ, 435, 536, arXiv:astro-ph/9402071
 Crocce, M., Pueblas, S., & Scoccimarro, R. 2006, MNRAS, 373, 369, arXiv:astro-ph/0606505
 Crocce, M., & Scoccimarro, R. 2006, Phys. Rev. D, 73, 063520, arXiv:astro-ph/0509419
 Falck, B. L., Neyrinck, M. C., Aragon-Calvo, M. A., Lavaux, G., & Szalay, A. S. 2012a, ApJ, 745, 17, 1111.4466
 Falck, B. L., Neyrinck, M. C., & Szalay, A. S. 2012b, ApJ, 754, 126, 1201.2353
 Fosalba, P., & Gaztañaga, E. 1998, MNRAS, 301, 503, arXiv:astro-ph/9712095
 Fosalba, P., & Gaztañaga, E. 1998, MNRAS, 301, 535, arXiv:astro-ph/9802165
 Fry, J. N., & Scherrer, R. J. 1994, ApJ, 429, 36
 Hidding, J., van de Weygaert, R., Vegter, G., Jones, B. J. T., & Teillaud, M. 2012, ArXiv e-prints, 1205.1669
 Jasche, J., & Wandelt, B. D. 2012, ArXiv e-prints, 1203.3639
 Kitaura, F.-S., & Angulo, R. E. 2012, MNRAS, 425, 2443, 1111.6617
 Kofman, L., Pogosyan, D., Shandarin, S. F., & Melott, A. L. 1992, ApJ, 393, 437
 Kofman, L. A., & Shandarin, S. F. 1988, Nature, 334, 129
 Manera, M. et al. 2012, MNRAS, submitted, 1203.6609
 McCullagh, N., & Jeong, D. in prep
 Melott, A. L., Pellman, T. F., & Shandarin, S. F. 1994, MNRAS, 269, 626, arXiv:astro-ph/9312044
 Mohayaee, R., Mathis, H., Colombi, S., & Silk, J. 2006, MNRAS, 365, 939, arXiv:astro-ph/0501217
 Monaco, P., Theuns, T., & Taffoni, G. 2002, MNRAS, 331, 587, arXiv:astro-ph/0109323
 Neyrinck, M. C. 2012, MNRAS, in press, 1202.3364
 Neyrinck, M. C., Gnedin, N. Y., & Hamilton, A. J. S. 2005, MNRAS, 356, 1222, arXiv:astro-ph/0402346
 Neyrinck, M. C., & Szapudi, I. 2008, MNRAS, 384, 1221, 0710.3586
 Neyrinck, M. C., Szapudi, I., & Szalay, A. S. 2009, ApJL, 698, L90, 0903.4693
 Peebles, P. J. E. 1980, The large-scale structure of the universe (Princeton, N.J., Princeton University Press, 1980. 435 p.)
 Platen, E., van de Weygaert, R., & Jones, B. J. T. 2007, MNRAS, 380, 551, 0706.2788
 Protogeros, Z. A. M., & Scherrer, R. J. 1997, MNRAS, 284, 425, arXiv:astro-ph/9603155 (PS97)
 Sahni, V., & Shandarin, S. 1996, MNRAS, 282, 641, arXiv:astro-ph/9510142
 Schaap, W. E., & van de Weygaert, R. 2000, A&A, 363, L29, arXiv:astro-ph/0011007
 Scherrer, R. J., & Gaztañaga, E. 2001, MNRAS, 328, 257, arXiv:astro-ph/0105534
 Scoccimarro, R. 1998, MNRAS, 299, 1097, arXiv:astro-ph/9711187
 Scoccimarro, R., & Sheth, R. K. 2002, MNRAS, 329, 629, arXiv:astro-ph/0106120

- Serra, J. 1983, *Image Analysis and Mathematical Morphology* (Orlando, FL, USA: Academic Press, Inc.)
- Shandarin, S., Habib, S., & Heitmann, K. 2012, *Phys. Rev. D*, 85, 083005, 1111.2366
- Shandarin, S. F. 2009, *ArXiv e-prints*, 0912.4520
- Springel, V. 2005, *MNRAS*, 364, 1105, arXiv:astro-ph/0505010
- Tassev, S., & Zaldarriaga, M. 2012, *JCAP*, 4, 13, 1109.4939
- Tatekawa, T., & Mizuno, S. 2007, *JCAP*, 12, 14, 0706.1334
- Valageas, P., & Bernardeau, F. 2011, *Phys. Rev. D*, 83, 043508, 1009.1974
- van de Weygaert, R., & Schaap, W. 2009, in *Data Analysis in Cosmology*, ed. V. Martinez, E. Saar, E. Martnez-Gonzles, & M.-J. Pons-Bordera (Berlin: Springer), arXiv:0708.1441
- Zel'dovich, Y. B. 1970, *A&A*, 5, 84